MRS Communications (2026) 16:1338–1349
© The Author(s), under exclusive licence to The Materials Research Society, 2026
https://doi.org/10.1557/s43579-026-01047-1

MRS Communications

Early Career Materials Researcher Research Letter

CALPHAD-based analysis of solidification properties and crack susceptibility in superalloys

Mohammad Younes Araghi, and Shuozhi Xu, School of Aerospace and Mechanical Engineering, University of Oklahoma, Norman, OK 73019, USA
Address all correspondence to Shuozhi Xu at **shuozhixu@ou.edu**

(Received 13 May 2026; accepted 1 September 2026; published online: 17 September 2026)

Abstract

Solidification cracking limits the welding, casting, and additive manufacturing of superalloys. Here, equilibrium and Scheil solidification calculations were performed for 555 literature-derived Ni-, Co-, and Fe-based superalloys using CALPHAD. Calculated properties include liquidus and solidus temperature, freezing range, γ'-related phase-stability, and crack susceptibility coefficients based on the Clyne–Davies, Kou, and Easton models. Fe-based alloys show the highest average freezing range and crack susceptibility, whereas Co-based alloys show the lowest. Correlation analysis identifies key elemental effects on cracking tendency. It is suggested that solidification properties may guide alloy processability assessment before experimental processing.

Introduction

Superalloys are essential high-temperature structural materials because they retain mechanical strength, oxidation resistance, creep resistance, and microstructural stability under demanding service conditions.[1] Ni-based superalloys are especially important in gas turbines, aerospace propulsion systems, power-generation components, and other environments where conventional alloys cannot maintain sufficient performance at elevated temperatures.[2] Recent studies have also expanded the concept of superalloys to multi-principal-element superalloys (MPESAs); examples of which include CrCoNi-based medium entropy superalloys,[3] Fe–Ni-base MPESAs with coherent γ/γ' microstructures,[4] directionally solidified MPESAs,[5] single-crystalline MPESAs,[6] and Co–Fe–Ni-based MPESAs processed by laser powder-bed fusion.[7] These emerging alloy classes broaden the traditional Ni-, Co-, and Fe-based superalloy design space and motivate a composition classification approach that can handle alloys with comparable amounts of multiple base elements. In addition to conventional casting, forging, and welding, recent advances in metal additive manufacturing have increased interest in processing superalloys into complex geometries with reduced material waste and improved design flexibility.[8,9] However, many high-performance superalloys remain difficult to process because alloy compositions optimized for high-temperature strength are often susceptible to solidification cracking.

Solidification cracking, often referred to as hot cracking in welding and additive manufacturing, occurs during the final stages of solidification when liquid films remain along interdendritic regions or grain boundaries, while thermal contraction and mechanical strain develop in the semi-solid material. This phenomenon depends on the solidification-temperature range, the evolution of solid fraction with temperature, solute segregation, terminal liquid feeding, grain-boundary wetting, and the ability of the mushy zone to accommodate strain before complete solidification.[10] In superalloys, the problem is particularly complex because alloying elements such as Al, Ti, Nb, Ta, Mo, W, Re, and Hf can strongly affect phase stability, segregation behavior, liquidus and solidus temperatures, and the persistence of terminal liquid.

Several metrics have been proposed to quantify hot tearing or solidification cracking tendency. Freezing range (FR) is the simplest metric and has been used as a crack-proneness indicator in computational alloy design.[11] More detailed crack susceptibility criteria, including the Clyne–Davies, Kou, and Easton models, use the calculated solidification path to describe the vulnerable region near the end of solidification.[12] These criteria do not necessarily provide identical rankings because each emphasizes a different aspect of the terminal solidification path. Therefore, comparing the FR with multiple crack susceptibility coefficients (CSC) can provide a more complete view of the calculated cracking tendency. Correlations among these properties are also important because they can reveal whether simple quantities such as FR are sufficient, or more detailed terminal solidification metrics are needed.

The CALculation of PHAse Diagrams (CALPHAD) method provides a practical approach for linking multicomponent alloy composition to phase stability and solidification behavior. CALPHAD describes the Gibbs energy of phases using assessed thermodynamic models and enables calculations of phase equilibria and solidification paths in multicomponent systems.[13] In the context of solidification cracking, Scheil calculations are especially useful because they approximate solute redistribution during non-equilibrium solidification and provide the relationship between temperature and solid fraction, $T(f_s)$ or $f_s(T)$, needed to evaluate crack susceptibility criteria, where

f_s denotes the fraction of the alloy that has solidified at a given temperature T. Although the classical Scheil model neglects diffusion in the solid and assumes complete mixing in the liquid, it remains useful as a consistent comparison framework for studying solidification behavior across many alloy compositions.

A central question is whether simple solidification properties, such as FR, are sufficient to describe crack susceptibility, or whether more detailed CSC formulations are needed. Correlation analysis among liquidus temperature, solidus temperature, FR, γ′-related properties, alloy composition, and CSC metrics can clarify which quantities contain overlapping information and which capture distinct aspects of late-stage solidification behavior. Here, late-stage solidification refers to the high-solid-fraction mushy-zone region where the remaining liquid exists between dendrites or grains, and solidification cracking is most likely to develop. This provides the motivation for comparing not only family-level averages but also correlations among calculated properties and composition–CSC correlations.

In this work, CALPHAD-based equilibrium and classical Scheil calculations were performed for 555 literature-derived Ni-, Co-, and Fe-dominant superalloy compositions. The main contribution is not the introduction of a new thermodynamic or crack susceptibility model, but the development of a consistent comparative framework in which all compositions are evaluated using the same database, calculation conditions, normalization procedure, and post-processing approach. This framework enables direct comparison of liquidus and solidus temperatures, FR, γ′-related phase stability, and calculated crack susceptibility across the three alloy families. It also includes conventional and MPESA-classified compositions and compares the Clyne–Davies, Kou, and Easton CSC formulations side by side, providing a unified dataset-level assessment of composition-dependent trends in terminal solidification behavior.

Methodology and materials

This section describes the composition collection, alloy classification, CALPHAD equilibrium calculations, classical Scheil solidification calculations, and crack susceptibility metrics used in this work. The workflow was designed to ensure that all Ni-, Co-, and Fe-based superalloys were processed under the same thermodynamic calculation framework, so that the calculated solidification properties and CSC could be compared consistently across alloy families.

Superalloy composition collection and standardization

A total of 555 nominal superalloy compositions were considered in this work. The compositions were not randomly sampled; they were collected from published superalloy literature and reported alloy composition tables. The sources include Co-based γ/γ′ superalloys, additively manufacturable superalloy design studies, single-crystalline Ni-based superalloys, and representative commercial or classical superalloys.[2,14–22] These references were used to define realistic reported compositions rather than artificial compositions generated by random sampling. The dataset is provided through Zenodo (see the link in the Data Availability section).

The dataset was assembled from compositions already reported in the literature and was not balanced by design. As a result, the three family subsets differ substantially in size: 223 Ni-based, 302 Co-based, and 30 Fe-based compositions. The Co-based subset is the largest because γ/γ′ Co-based superalloy design has been an active area of computational alloy design, and the available composition databases are accordingly larger. The Fe-based subset is the smallest. Near-duplicate or highly similar compositions were not explicitly removed because the dataset represents the spread of reported compositions in the superalloy literature; however, the imbalance means that family-level statistics, particularly those involving the Fe-based group, should be interpreted with caution (see also "Results and discussion" section). The mixture of commercial alloys and design-study compositions within each family could also influence the statistical comparison, since design-study compositions may occupy a more unusual region of the alloy composition space than classical commercial grades.

The raw compositions were standardized in weight percent because most reported superalloy compositions are given in wt%. Each composition was organized into a fixed elemental format for CALPHAD calculation, and elements not present in a given alloy were assigned a value of zero. The elemental set includes Ni, Co, Fe, Cr, Al, Ti, Mo, W, Nb, Ta, Re, Hf, V, Zr, B, C, Ru, and Si. These elements were selected because they are commonly used in superalloy design and can influence oxidation resistance, γ′ stability, solid-solution strengthening, segregation, liquidus temperature, solidus temperature, and FR.

For the family-level analysis, each alloy was classified according to the dominant base element among Ni, Co, and Fe. Therefore, an alloy was labeled Ni-based, Co-based, or Fe-based if Ni, Co, or Fe had the largest concentration among the three base elements. A strict > 50% threshold was not imposed because several MPESAs do not contain a majority base element, and some compositions in the present dataset contain more than one base element at tens of wt%. For example, one of the alloys contains 46.26 wt% Ni and 23.3 wt% Co; it is therefore classified as Ni-based because Ni is the largest base-element concentration, even though Ni is below 50 wt%. No separate mixed-base category was used in the present analysis because the goal was to compare broad Ni-, Co-, and Fe-dominant families consistently. This dominant-element classification produced 223 Ni-based, 302 Co-based, and 30 Fe-based compositions.

The composition set also contains alloys that satisfy a quantitative MPESA definition. In the multi-principal-element alloy (MPEA) literature, principal elements are commonly defined using atomic-percentage ranges, often 5–35 at.%, while MPEAs are generally described as alloys containing three or more principal elements in significant amounts.[23] Because

conventional superalloys may contain several alloying additions above 5 at.% while still having one dominant base element, a stricter MPESA criterion was used here: at least three elements in the 5–35 at.% range and no single element above 50 at.%. Based on this criterion, the wt% compositions were converted to at.% for MPESA classification and identified 81 of the 555 alloys as MPESAs.

CALPHAD

In the CALPHAD approach, phase stability is evaluated by minimizing the total Gibbs energy of a multicomponent and multiphase system under mass-balance constraints. For a system containing several possible phases, the equilibrium state can be written in a general form as

$$G^{\mathrm{sys}}(T,P,\mathbf{x}) = \min_{\{n^{\phi},y_i^{\phi}\}} \sum_{\phi} n^{\phi} G_m^{\phi}\left(T,P,\{y_i^{\phi}\}\right), \qquad (1)$$

where G^{sys} is the total Gibbs energy of the system, ϕ denotes a phase, n^{ϕ} is the number of moles of phase ϕ, G_m^{ϕ} is the molar Gibbs energy of phase ϕ, and y_i^{ϕ} represents the composition variable of component i in phase ϕ. At equilibrium, the chemical potentials of each component are equal among all coexisting phases, while the overall alloy composition is conserved. In the present implementation, this Gibbs-energy minimization was carried out using Thermo-Calc 2024a with the TCNI12 thermodynamic database.[24]

We note that the TCNI12 database is primarily developed and validated for Ni-based superalloy compositions. Its binary and ternary subsystem assessments are most extensive for Ni-rich systems; Co- and Fe-containing subsystems that do not involve Ni as a dominant component may have fewer directly assessed ternary interactions. That said, the Co-based alloys in this dataset are all γ/γ' Co–Ni–Cr–W or related systems with significant Ni content; in the literature, TCNI12 has been applied to some of these alloys for solidification calculations and is expected to provide reliable results.[14] For the 30 Fe-based compositions, which include alloys with substantial Fe and lower Ni content, the thermodynamic descriptions of Fe-rich subsystems in TCNI12 may be less thoroughly assessed than those for Ni-rich systems. Therefore, the absolute calculated values for Fe-based alloys, particularly the FRs and CSCs, should be interpreted cautiously, as they may partly reflect database extrapolation rather than absolute metallurgical differences. Instead, the relative ordering within the Fe-based subset and the qualitative comparison with the Ni- and Co-based subsets should be considered more valuable. To assess the effect of database selection on the simulation results, we compared the TCNI12 and TCHEA7 databases for all 81 MPESAs; this comparison is presented in section "Conventional superalloys and MPESAs comparison".

Equilibrium calculations were used to evaluate phase stability and extract phase-related properties. The main phase quantities analyzed in this work were the γ' solvus-related property and the γ' phase-fraction property because γ' is a central strengthening phase in many Ni-based and Co-based γ/γ' superalloys.[25] The γ' solvus temperature was determined from the equilibrium temperature-step calculations as the highest temperature at which the ordered $L1_2$ phase (FCC_L12 in TCNI12 notation) appears with a nonzero mole fraction. The γ' phase-fraction property was extracted from the equilibrium phase-fraction curve averaged over the temperature range 800–1100°C. This averaging range was selected because it encompasses the typical service and heat-treatment temperature window for many γ/γ' superalloys and captures the overall stability of the precipitate phase rather than a value at a single temperature. These equilibrium quantities are interpreted as phase-stability indicators and are not derived from the Scheil solidification path. However, γ' is not the only strengthening or microstructurally important phase in superalloys. In Nb-containing Ni-based superalloys such as Inconel 718, strengthening can be dominated by metastable γ''-Ni_3Nb precipitates, and recent alloy design studies have also explored dual γ'/γ'' strengthening strategies. Other phases, including the γ matrix, δ-Ni_3Nb, carbides, borides, and topologically close-packed phases, may also influence mechanical properties, phase stability, and processability depending on alloy composition and thermal history.[26] Therefore, the γ'-related quantities reported here should be interpreted as selected phase-stability indicators rather than a complete description of all possible precipitate or secondary phases.

Classical Scheil solidification calculations

Classical Scheil calculations were used to approximate non-equilibrium solidification behavior. The classical Scheil model assumes complete mixing in the liquid, negligible diffusion in the solid, and local equilibrium at the solid–liquid interface.[27] Under these assumptions, the composition of the remaining liquid phase evolves continuously as solidification proceeds, while each newly formed solid increment is removed from further diffusion. In a multicomponent alloy, the liquid composition is therefore a composition vector, $\mathbf{x}^{\mathrm{L}}(f_s)$, whose components represent the fractions of each element remaining in the liquid at a given solid fraction f_s. This liquid composition is generally different from the nominal alloy composition after solidification begins because solute redistribution enriches or depletes different elements in the remaining liquid. In CALPHAD-based Scheil calculations, this process is treated numerically by repeatedly calculating local equilibrium between the uniform liquid and the possible solid phases as temperature decreases.

All Scheil calculations in this work used the classical Scheil formulation without back-diffusion corrections. The fast-diffusing interstitial elements B, C, and N were treated as classical Scheil solutes (no back-diffusion).[12] This choice has a caveat: in alloys containing B and C, the classical Scheil model predicts strong terminal liquid enrichment in these interstitials, which can produce long low-temperature liquid tails near complete solidification. The solid-fraction range $f_s = 0.90$ to $= 0.99$ that governs the numerator of the

Clyne–Davies criterion and the near-unity region of the Kou criterion is therefore most directly affected by this assumption. If back-diffusion of B or C were allowed, the terminal solidification interval and the CSC values for B- and C-containing alloys would be expected to decrease. Because B and C are present in only 84 out of the 555 alloys and at minor concentrations (typically below 0.1 wt%), this effect is expected to shift the absolute CSC values only for a subset of alloys rather than change the overall family-level ranking. The calculated CSC values for B- or C-containing alloys should therefore be interpreted as upper bounds on cracking tendency relative to the same compositions treated with partial back-diffusion. The calculation was terminated at $f_s = 0.99$, which serves as the practical endpoint for solidification in all CSC evaluations. Beyond this solid fraction, the remaining 1% liquid is treated as non-solidifying for the purposes of the Scheil path used in CSC extraction.

The liquidus temperature, T_{liq}, was obtained from the calculated solidification path as the temperature at which the first non-liquid phase appears during cooling. Equivalently, it is the highest temperature at which the calculation predicts a nonzero solid fraction. The solidus temperature, T_{sol}, was obtained from the end of the calculated solidification path. For crack susceptibility analysis, the end of solidification is commonly represented by a high solid fraction close to complete solidification, such as $f_s = 0.99$, because the final small amount of liquid is most relevant to terminal liquid films and hot tearing.[11] The FR was then calculated as

$$\mathrm{FR} = T_{liq} - T_{sol}. \tag{2}$$

A larger FR indicates that the alloy remains in the semi-solid mushy zone over a wider temperature interval. This can increase the persistence of thin residual liquid layers between dendrites or along grain boundaries near the end of solidification and reduce the ability of liquid feeding to compensate for thermal contraction and solidification shrinkage. For this reason, FR has been used as a simple crack-proneness indicator in computational design of printable superalloys.[11]

Crack susceptibility metrics

CSCs were obtained from the CALPHAD/Scheil solidification path using the built-in CSC model. The three metrics considered in this work were the Clyne–Davies, Kou, and Easton coefficients. Public documentation for the CSC model states that the model uses the Scheil calculator and allows the user to choose among the Clyne–Davies, Kou, and Easton models. Because the internal numerical implementation may include software-specific interpolation and endpoint handling, the equations below are presented as the literature basis of the selected models rather than as an independent reimplementation of the software output.

The Clyne–Davies criterion[10] compares the vulnerable terminal solidification interval with the earlier interval over which liquid feeding and stress relaxation are possible. In its commonly reported form, the CSC is written as

$$\mathrm{CSC_{CD}} = \frac{t_{0.99} - t_{0.90}}{t_{0.90} - t_{0.40}}\ (\text{dimensionless}), \tag{3}$$

where $t_{0.40}$, $t_{0.90}$, and $t_{0.99}$ are the times at which the solid fraction reaches 0.40, 0.90, and 0.99, respectively. The numerator represents the vulnerable terminal solidification interval, while the denominator represents the earlier interval over which feeding and stress relaxation are more effective. Therefore, the Clyne–Davies coefficient is a dimensionless ratio. When the cooling rate is assumed to be approximately constant, this time ratio can be expressed using temperatures extracted from the calculated solidification path:

$$\mathrm{CSC_{CD}} \approx \frac{T_{0.90} - T_{0.99}}{T_{0.40} - T_{0.90}}\ (\text{dimensionless}), \tag{4}$$

where $T_{0.40}$, $T_{0.90}$, and $T_{0.99}$ are the temperatures corresponding to solid fractions of 0.40, 0.90, and 0.99, respectively. This form has been widely used to estimate composition-dependent hot-tearing tendency from calculated solidification curves.[10,11]

The Kou criterion[28] describes crack susceptibility using the steepness of the temperature–fraction–solid curve near the end of solidification. Its literature form is commonly written as

$$\mathrm{CSC_{Kou}} = \left| \frac{\mathrm{d}T}{\mathrm{d}\left(f_s^{1/2}\right)} \right|_{f_s^{1/2} \to 1} (^\circ\mathrm{C}). \tag{5}$$

Because f_s is dimensionless, the Kou coefficient has units of temperature and is reported here in °C. A larger terminal slope indicates that liquid channels remain open over a wider temperature interval near high solid fraction, which increases the tendency for solidification cracking. This criterion has been used with Scheil-type solidification calculations to evaluate crack susceptibility in alloy design and additive-manufacturing studies.[11,28]

In practice, the limit $f_s^{1/2} \to 1$ is evaluated numerically over a finite high-solid-fraction interval. In the present implementation, the terminal slope is extracted from the Scheil solidification path in the range $f_s = 0.90$ to $= 0.99$ (i.e., $f_s^{1/2}$ from approximately 0.949 to 0.995), consistent with the region where liquid-film persistence and hot tearing are most likely.[11,28]

The Easton criterion[29] is an a priori hot-tearing indicator based on the area under the solid-fraction curve between coherency and coalescence. A general form can be written as

$$\mathrm{CSC_{Easton}} = \int_{T_{coal}}^{T_{coh}} f_s(T)\,\mathrm{d}T\ (^\circ\mathrm{C}), \tag{6}$$

where T_{coh} is the temperature at which feeding becomes restricted by coherency, and T_{coal} is the temperature at which a three-dimensional solid network forms by coalescence. Because f_s is dimensionless and the integration is performed with respect to temperature, the Easton coefficient has units of temperature and is reported here in °C. Easton et al.[29]

proposed this type of integral indicator because hot tearing depends on the amount of solid present over the vulnerable semi-solid interval, not only on the total FR. In practice, the selected coherency and coalescence limits can influence the numerical value of the Easton index; therefore, the present work uses the built-in CALPHAD/Scheil implementation consistently for all compositions.

Previous reviews and methodology studies have emphasized that hot-tearing and solidification-cracking indices, including Clyne–Davies, Kou, and Easton-type criteria, provide relative susceptibility measures rather than universal crack/no-crack thresholds.[12,30] Therefore, the CSC values in this work are interpreted as relative indicators of terminal solidification vulnerability. They should not be interpreted as direct experimental crack length, crack density, or absolute cracking probability. Comparing the three CSC formulations is useful because each one emphasizes a different aspect of the terminal solidification path.

The Clyne–Davies, Kou, and Easton coefficients are used here as relative solidification-path features for preliminary screening, not as direct or experimentally validated predictions of cracking. Higher values indicate a comparatively less favorable terminal solidification path according to each criterion; however, actual cracking also depends on factors not included in the present calculations, such as grain structure, liquid feeding, thermal gradient, cooling rate, local strain, residual stress, and processing conditions.

Results and discussion

The calculated results were analyzed to compare composition, CALPHAD-derived properties, and crack susceptibility trends among Ni-, Co-, and Fe-based superalloys. The analysis focuses on whether these alloy families show systematic differences in solidification behavior and calculated cracking tendency.

All CALPHAD-derived quantities were reported first in their physical units (temperatures in Kelvin, CSC values as dimensionless ratios or their respective units). For multi-property comparison plots and correlation analyses where quantities with different units appear together, a min–max normalization was applied:

$$x_{\mathrm{norm}} = \frac{x - x_{\mathrm{min}}}{x_{\mathrm{max}} - x_{\mathrm{min}}}, \tag{7}$$

where the minimum and maximum are taken over all 555 alloys in the full dataset. This normalization places all properties on a common [0, 1] scale for visualization purposes only and does not affect the physical interpretation of the values. Where specific values are cited in the text, they refer to min–max-normalized values unless explicitly stated otherwise; for example, the average FRs reported in this section (0.115 for Co-based, 0.274 for Ni-based, and 0.343 for Fe-based alloys) are normalized values.

Compositions among alloy families

The composition-family comparison is summarized in Fig. 1. The dataset contains 223 Ni-based, 302 Co-based, and 30 Fe-based compositions, indicating a substantial imbalance among the three alloy families. The Co-based subset is the largest, whereas the Fe-based subset is considerably smaller. Therefore, correlations calculated for the Fe-based group should be interpreted cautiously because they are based on fewer compositions.

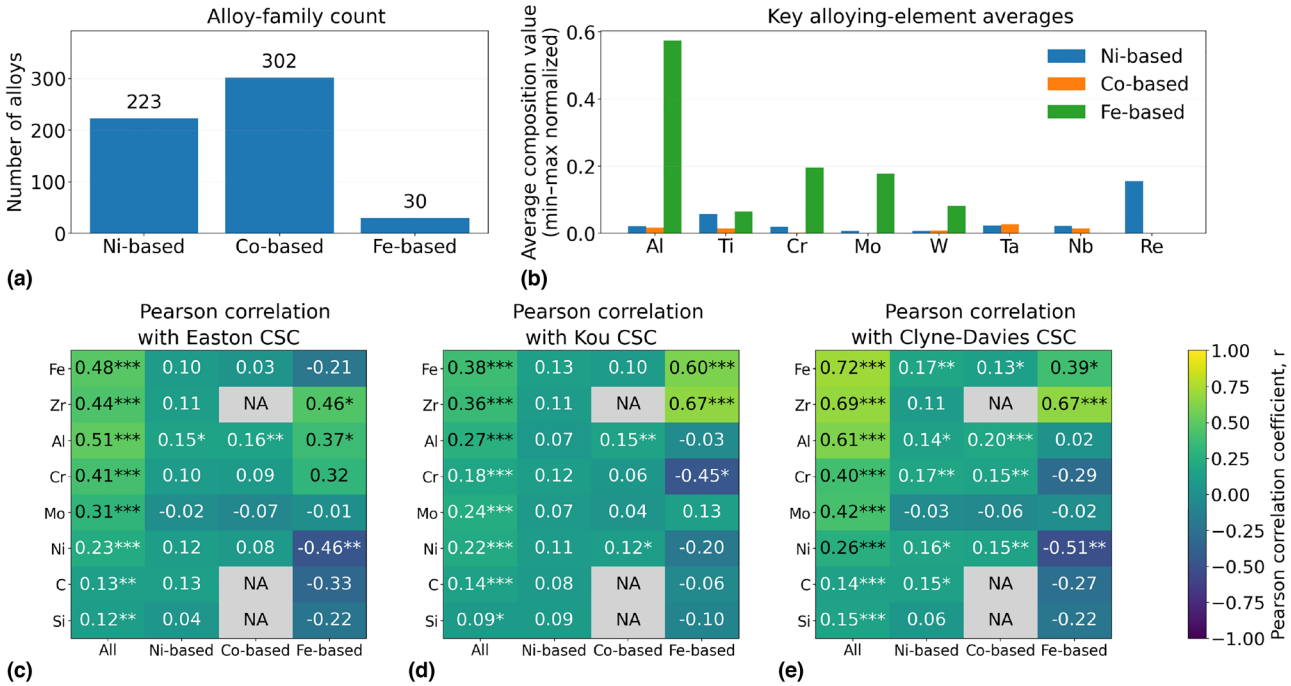
As shown in Fig. 1(b), the Fe-based compositions contain substantially higher normalized Al, Cr, Mo, and W values than the Ni- and Co-based subsets. The Ni-based group shows comparatively higher Ti, Nb, and particularly Re values, whereas the Co-based group generally exhibits lower average values for most of the selected alloying elements. These bars represent min–max-normalized composition values and should therefore be interpreted as relative family-level trends rather than absolute wt% concentrations.

Panels (c)–(e) present Pearson correlations separately for the Easton, Kou, and Clyne–Davies CSC metrics, avoiding the use of an averaged CSC. Here, r is the Pearson correlation coefficient, which indicates the strength and direction of the linear relationship. For all alloys, Al, Fe, Zr, and Cr show positive correlations with the three CSC metrics. The strongest overall relationships are observed for the Clyne–Davies CSC, particularly for Fe ($r = 0.72$), Zr ($r = 0.69$), and Al ($r = 0.61$). Easton CSC is most strongly associated with Al ($r = 0.51$), Fe ($r = 0.48$), and Zr ($r = 0.44$), whereas Kou CSC shows weaker overall correlations, led by Fe ($r = 0.38$) and Zr ($r = 0.36$).

Within the individual families, most correlations in the Ni-based and Co-based subsets are relatively weak. In contrast, the Fe-based subset shows stronger element-specific relationships, including positive correlations of Zr with all three CSC metrics and Fe with Kou and Clyne–Davies CSC. Ni is negatively correlated with Easton and Clyne–Davies CSC in the Fe-based subset, while Cr shows a negative correlation with Kou CSC. These family-specific trends should be interpreted as associations within the present dataset rather than direct evidence of causation.

Family-level non-CSC properties

In what follows, the solidus temperature, liquidus temperature, FR, γ' solvus-related property, and γ' phase-fraction property are collectively referred to as non-CSC properties. This term is used only to distinguish these CALPHAD-derived solidification and phase-stability properties from the CSC metrics discussed in the next subsection. The solidus and liquidus temperatures define the calculated solidification-temperature interval, the FR describes the width of this interval, and the γ'-related quantities describe selected phase-stability trends. These quantities are therefore useful for interpreting the calculated CSC trends, but they are not themselves CSC metrics. Figure 2 compares the CALPHAD-derived solidification and phase-stability properties, including normalized solidus



NA: insufficient variation or sample size; * p<0.05, ** p<0.01, *** p<0.001. The same data-selected elements are shown in panels (c)–(e).

Figure 1. Composition and crack susceptibility summary: (a) alloy-family count, (b) average min–max-normalized values of selected alloying elements; and Pearson correlations between elemental composition and (c) Easton CSC, (d) Kou CSC, and (e) Clyne–Davies CSC. The same data-selected elements are shown in panels (c)–(e). Cells marked as NA indicate insufficient sample size or insufficient compositional variation. Statistical significance is indicated by $^{*}p < 0.05$, $^{**}p < 0.01$, and $^{***}p < 0.001$.

temperature, liquidus temperature, FR, γ′ solvus property, and γ′ phase-fraction property.

The solidification-temperature properties reveal clear family-level differences. Ni-based alloys show the highest average normalized solidus and liquidus temperatures, indicating that they occupy the highest calculated solidification-temperature range among the three families. The freezing-range trend is different: Co-based alloys show the smallest average FR (0.115), followed by Ni-based alloys (0.274), while Fe-based alloys show the highest average FR (0.343). Therefore, the Co-based subset has the narrowest calculated mushy-zone interval, whereas the Fe-based subset remains semi-solid over the broadest temperature interval during solidification. This distinction is important because a wider FR is commonly associated with a broader mushy zone, more persistent terminal liquid films, and greater sensitivity to feeding difficulty during late-stage solidification.[11,30] The higher FR of the Fe-based subset is therefore consistent with its higher calculated CSC values discussed below, while the lower FR of the Co-based subset is consistent with its lower calculated crack susceptibility.

However, because the Fe-based group contains only 30 compositions, the error bars in Fig. 2(a) (representing one standard deviation within each family) are wider relative to the family average than for the Ni- and Co-based subsets. This means that the reported average FR and CSC values for Fe-based alloys carry higher uncertainty, and the trend identified here should be interpreted as specific to the present dataset rather than as a general statement about all Fe-based superalloys.

The freezing-range distribution further supports this trend. The Fe-based group shows a higher median FR than the Co-based group, while the Ni-based group shows a broader spread and several high-freezing-range outliers. Thus, although Fe-based alloys have the highest average FR, some Ni-based compositions also exhibit wide calculated solidification intervals. This is important because FR is useful as a first-order indicator of solidification cracking tendency but does not fully represent terminal solidification behavior.

The γ′-related properties show another clear family-level difference. Co-based alloys exhibit the highest average γ′ solvus-related property and γ′ phase-fraction property, while Fe-based alloys show the lowest values for both. Ni-based alloys show a high γ′ solvus-related value but a lower average γ′ phase fraction than Co-based alloys. This trend is consistent with the growing interest in Co-based γ/γ′ superalloys, where stabilizing the $L1_2$ γ′ phase is a central design objective.[14,25] In the present calculations, the Co-based subset combines high γ′-related values with relatively low FRs. We note that high γ′-related values indicate favorable calculated strengthening-phase stability, whereas a low FR suggests a narrower mushy-zone interval and lower sensitivity to late-stage liquid-film persistence during solidification. Therefore, the Co-based subset shows a favorable calculated balance between γ′-related phase stability and solidification processability within the present composition space.

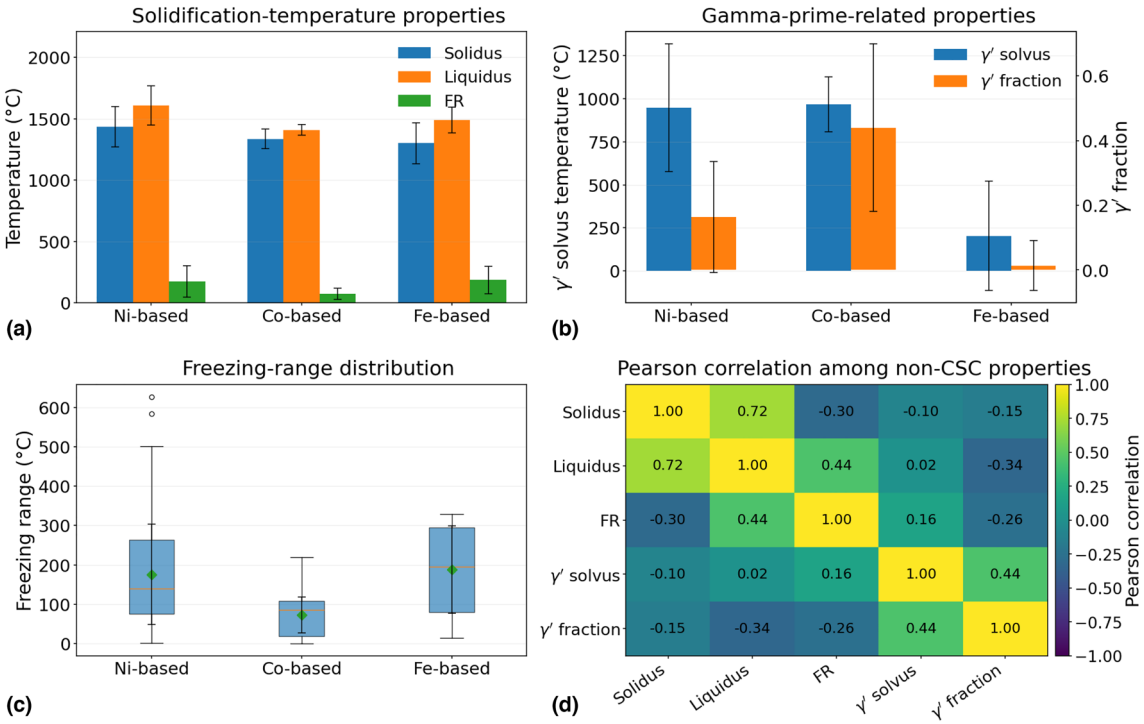


Figure 2. Non-CSC property analysis: (a) family-average solidification-temperature properties, (b) family-average γ′-related properties, (c) freezing-range distributions, and (d) Pearson correlations among non-CSC properties. All values are min–max normalized over the full dataset. In panels (a)–(c), error bars represent one standard deviation within each alloy family, providing a quantitative indication of the within-family spread, particularly for the smaller Fe-based subset. In panel (c), the diamond indicates the mean, the horizontal line indicates the median, and the box spans the interquartile range from the 25th to the 75th percentile. The whiskers extend to the most extreme observations lying within 1.5 times the interquartile range, while points beyond the whiskers represent individual outliers.

The correlation matrix in Fig. 2(d) shows that solidus and liquidus temperatures are strongly positively correlated, with a Pearson correlation coefficient of 0.72. FR is positively correlated with liquidus temperature and negatively correlated with solidus temperature, indicating that wide FRs arise from a combination of elevated liquidus values and reduced solidus values. The γ′ solvus-related property and γ′ phase-fraction property are also positively correlated. In contrast, γ′ fraction is negatively correlated with liquidus temperature and FR, suggesting that compositions with higher calculated γ′ fraction tend, on average, to show narrower FR in the present composition space.

These results indicate that the three alloy families differ not only in nominal composition but also in calculated phase stability and solidification behavior. Fe-based alloys show the least favorable combination of highest FR and lowest γ′ -related properties, whereas Co-based alloys show the lowest FR and the strongest calculated γ′-related phase stability. Ni-based alloys generally occupy an intermediate position with the highest solidification-temperature scale.

Crack susceptibility metrics and correlation analysis

The crack susceptibility trends and their relationships with composition and CALPHAD-derived solidification properties are summarized in Fig. 3. The figure compares family-average CSC metrics, the relationships between FR and each CSC metric, correlations between composition and non-CSC properties, and correlations between composition/non-CSC properties and CSC metrics.

The family-average CSC values in Fig. 3(a) show that Fe-based alloys have the highest average values for all three CSCs, while Co-based alloys have the lowest and Ni-based alloys fall between them. This consistent ordering across the Easton, Kou, and Clyne–Davies criteria indicates that the Fe-based subset has the least favorable calculated late-stage solidification behavior in the present composition space. Because the Fe-based group contains only 30 compositions, this trend should not be interpreted as a universal statement about all Fe-based superalloys; it reflects the compositions collected from the available literature for this study. The error bars in Fig. 3(a) (1 standard deviation within each family) make this uncertainty quantitative and show that the Fe-based family mean carries the highest statistical uncertainty.

Figure 3(b–d) compares FR with each CSC metric. The positive but scattered trends show that FR is a useful first-order indicator of crack susceptibility, but it is not sufficient to fully describe the calculated CSC values. This is expected because FR only measures the total liquidus–solidus temperature interval, whereas CSC metrics use additional information from the calculated solidification path, especially the evolution of solid

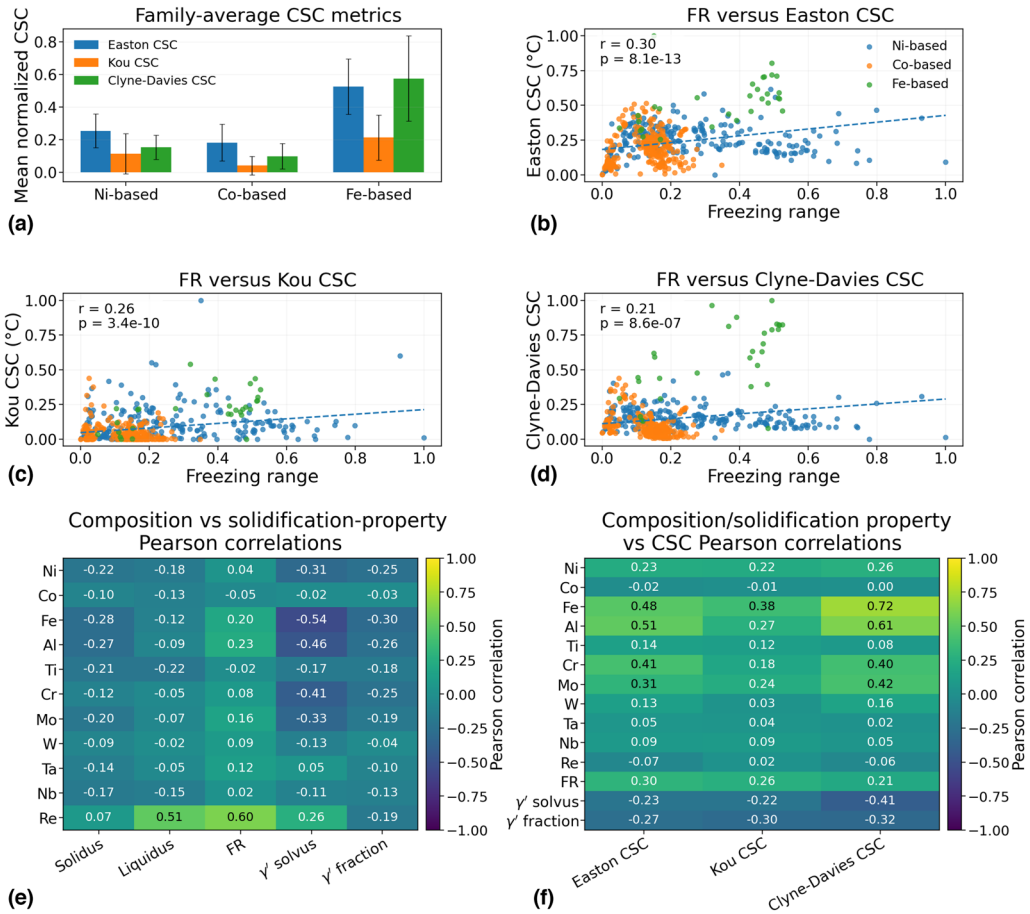


Figure 3. CSC analysis: (a) family-average CSC metrics with error bars representing one standard deviation within each family; relationships between FR and (b) Easton CSC, (c) Kou CSC, and (d) Clyne–Davies CSC; (e) correlations between composition and non-CSC properties; and (f) correlations between composition, selected non-CSC properties, and CSC metrics. The CSC values in panels (a)–(d) and the FR values in panels (b)–(d) are min–max normalized. Points in panels (b)–(d) are colored by alloy family. Error bars in panel (a) are particularly wide for the small Fe-based subset, reflecting the limited sample size and higher uncertainty in the family-average estimates.

fraction near the end of solidification. Previous studies have similarly connected cracking tendency to wide FRs, segregation, liquid feeding, and vulnerable residual liquid regions during late-stage solidification.[30]

The Pearson correlation maps in Fig. 3(e and f) further show that composition, non-CSC solidification properties, and CSC metrics are related but not interchangeable. In Fig. 3(e), Re shows a strong positive correlation with liquidus temperature and FR, while Fe and Al are associated with wider FRs and lower γ′-solvus-related values. In Fig. 3(f), Fe and Al show strong positive correlations with the Clyne–Davies CSC, whereas the γ′-related properties are negatively correlated with the CSC metrics. These trends suggest that calculated crack susceptibility is controlled by both alloy composition and the detailed shape of the solidification path.

Overall, Fig. 3 shows that FR provides useful but incomplete processability information. CALPHAD-derived CSC metrics provide a more detailed description because they account for late-stage solidification behavior beyond the total freezing interval. This conclusion is consistent with previous discussions of hot-tearing and solidification-cracking indices, which emphasize that individual criteria should be interpreted as relative susceptibility indicators rather than universal crack/no-crack thresholds.[30]

Conventional superalloys and MPESAs comparison

As described in "Superalloy composition collection and standardization" section, the collected compositions were separated into conventional and MPESA groups to examine whether the compositionally complex alloys occupy a distinct CALPHAD-derived property space. Among the 555 compositions, 81 were classified as MPESAs. As shown in Fig. 4(a), the dataset contains 22 Ni-based, 57 Co-based, and only 2 Fe-based MPESAs. The strong imbalance among the three families, particularly the very small Fe-based MPESA subset, should be considered when interpreting the family-level distributions.

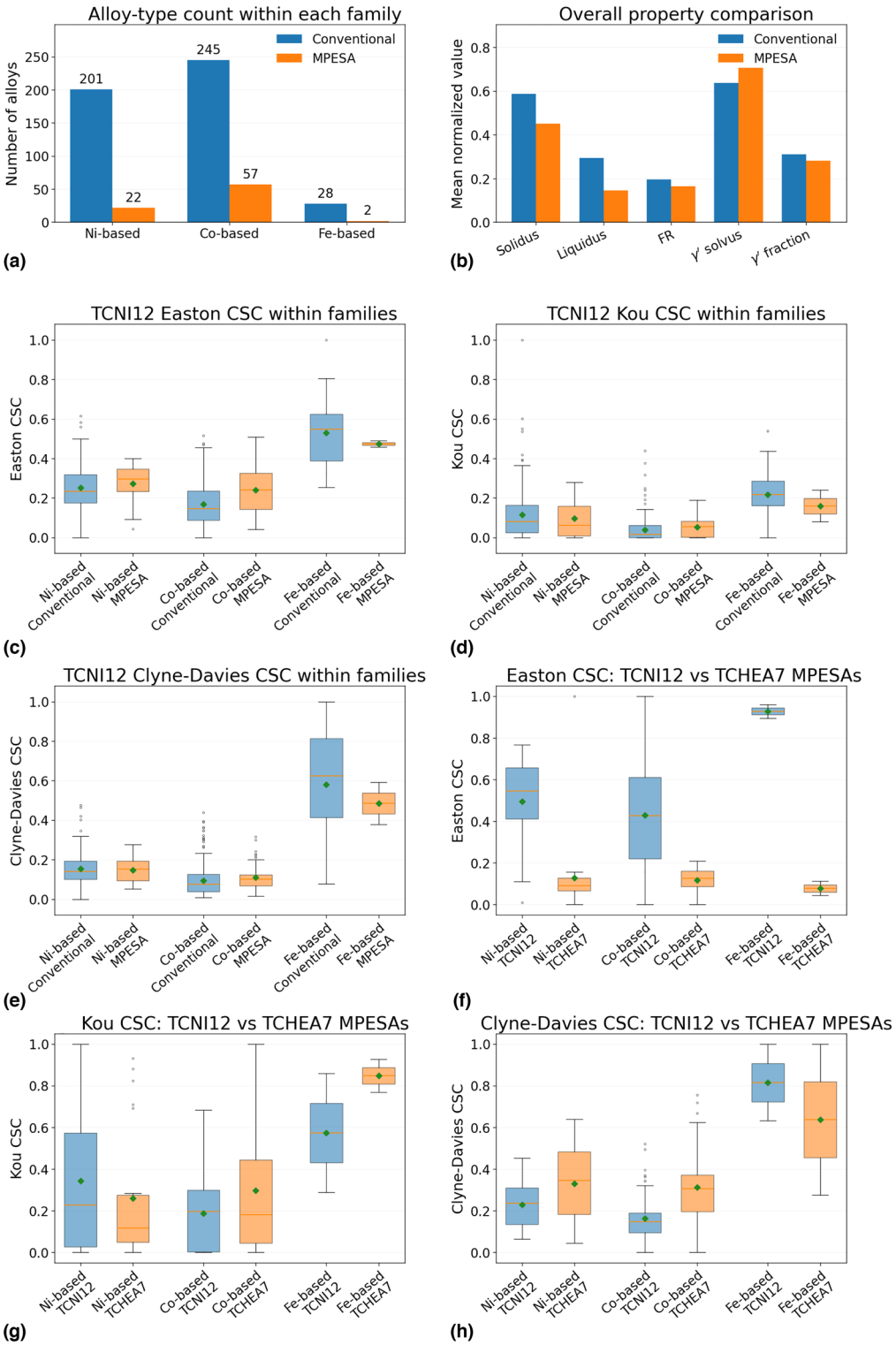


Figure 4. Comparison of conventional superalloys and MPESAs and evaluation of database sensitivity: (a) alloy counts within the Ni-, Co-, and Fe-based families; (b) overall mean normalized non-CSC properties; TCNI12-based distributions of (c) Easton, (d) Kou, and (e) Clyne–Davies CSC values for conventional and MPESA alloys; and normalized comparisons of the same 81 MPESAs calculated using TCNI12 and TCHEA7 for (f) Easton, (g) Kou, and (h) Clyne–Davies CSC. In the boxplots, diamonds indicate means, horizontal lines indicate medians, boxes represent interquartile ranges, whiskers extend to 1.5 times the interquartile range, and points beyond the whiskers are outliers.

The overall comparison in Fig. 4(b) indicates that the MPESA group has lower mean normalized solidus, liquidus, and freezing-range values than the conventional group. The MPESAs show a higher mean normalized γ′-solvus value, whereas their mean γ′ fraction is slightly lower. These results describe the compositions represented in the present dataset and should not be interpreted as universal characteristics of all MPESAs.

Panels (c)–(e) compare the TCNI12-based Easton, Kou, and Clyne–Davies CSC distributions between conventional and MPESA compositions within each alloy family. The differences depend on both the alloy family and the selected CSC formulation. For example, the Ni- and Co-based MPESA subsets show somewhat higher Easton CSC central values than their conventional counterparts, whereas the Kou and Clyne–Davies results show smaller or non-uniform differences. The Fe-based results display substantial variability and should be interpreted particularly cautiously because only two MPESAs are available in this family. Consequently, the results do not support a general conclusion that MPESAs are intrinsically more susceptible to solidification cracking than conventional superalloys.

To examine the sensitivity of the MPESA results to thermodynamic database selection, the same 81 MPESA compositions were additionally calculated using the TCHEA7 database and compared with their TCNI12 results in Fig. 4(f–h). The relative family-level distributions differ noticeably between the two databases, and the magnitude and direction of these differences depend on the CSC type. The Easton CSC results show the largest differences between TCNI12 and TCHEA7, while the Kou and Clyne–Davies metrics produce different database-dependent trends among the Ni-, Co-, and Fe-based subsets. Because each CSC metric was independently min–max normalized within each database, these panels assess changes in relative distributions and family rankings rather than differences in absolute CSC magnitudes.

The observed database sensitivity shows that calculated solidification paths and CSC values depend on the thermodynamic descriptions, Gibbs-energy parameters, assessed subsystems, and phase models contained in the selected database. TCNI12 was developed mainly for Ni-based superalloys and emphasizes Ni-rich systems and the γ/γ′ microstructure, whereas TCHEA7 was developed for broader MPE composition spaces and includes extensive descriptions of phases.[31–34] Therefore, the two databases may predict different phase stabilities, segregation behavior, terminal liquid compositions, and solidification temperatures, particularly for compositionally complex alloys containing strongly segregating minor or refractory elements. Since CALPHAD reliability generally decreases when predictions rely on extrapolation beyond well-assessed composition ranges,[35,36] the TCNI12–TCHEA7 comparison is used here to evaluate the robustness of the calculated trends rather than to identify one database as universally more accurate. Experimental data would be required to determine which description is more representative for a particular alloy; accordingly, the CSC values are treated as comparative screening descriptors rather than validated predictions of cracking.[28,29]

Conclusions

This work applied a consistent CALPHAD/Scheil framework to 555 literature-derived Ni-, Co-, and Fe-containing superalloy compositions to compare solidification behavior, γ′-related phase stability, and calculated CSC values. The analysis included liquidus temperature, solidus temperature, FR, γ′ solvus-related property, γ′ phase-fraction property, and CSC values based on the Easton, Kou, and Clyne–Davies criteria.

The three alloy families show distinct calculated trends. Ni-based alloys have the highest average solidus and liquidus temperatures. Co-based alloys combine the lowest average FR with the highest average γ′-related properties, suggesting a favorable balance between phase stability and solidification behavior. In contrast, Fe-based alloys show the highest average FR, the lowest γ′-related properties, and the highest average CSC values. Because the Fe-based subset contains only 30 compositions, this trend should be interpreted as specific to the present dataset rather than as a universal ranking of Fe-based superalloys.

Correlation analysis shows that FR is a useful but incomplete indicator of calculated crack susceptibility. Although wider FRs generally correspond to higher CSC values, the scatter in the FR–CSC relationships indicates that the detailed solidification path also matters. Composition also contributes strongly: Fe and Al show strong positive correlations with the Clyne–Davies CSC, while γ′-related properties are negatively correlated with the CSC metrics within the present composition space.

Among the 555 compositions, 81 satisfy the MPESA criterion. Their calculated properties differ according to alloy family, CSC formulation, and thermodynamic database, while only two Fe-based MPESAs are represented. Consequently, the present results do not support a general conclusion that MPESAs are intrinsically more susceptible to solidification cracking than conventional superalloys. Alloy family, detailed composition, database selection, and the selected CSC formulation remain important when interpreting these comparisons.

Overall, CALPHAD-derived solidification and phase-stability properties provide useful relative indicators for screening superalloy processability before experimental trials. The calculated CSC values should not be interpreted as direct measurements of crack length, crack density, or absolute cracking probability. Instead, they provide a consistent thermodynamic basis for comparing relative late-stage solidification vulnerability across a large composition space. This interpretation is consistent with Scheil-based CSC models, where Clyne–Davies, Kou, and Easton criteria are used as relative hot-tearing or solidification-cracking indicators rather than universal crack/no-crack thresholds.

Several limitations should be recognized. The results depend on the selected thermodynamic database, calculation settings, and classical Scheil assumptions, including complete liquid mixing and negligible solid diffusion. The present analysis also does not include process parameters such as cooling rate, thermal gradient, scan speed, laser power, hatch spacing, build geometry, or local strain accumulation. Future work should combine CALPHAD-derived quantities with experimental cracking data, process-specific simulations, broader phase-by-phase analysis, and interpretable machine-learning models to better connect composition, solidification behavior, processing conditions, and cracking response.

Author contributions

Mohammad Younes Araghi contributed toward conceptualization, methodology, software, data curation, formal analysis, visualization, and writing—original draft. Shuozhi Xu contributed toward conceptualization, supervision, methodology, writing—review and editing, and project administration.

Funding

Mohammad Younes Araghi expresses gratitude for receiving the Mathnasium Engineering Scholarship awarded by the University of Oklahoma.

Data availability

The calculated liquidus temperature, solidus temperature, FR, gamma-prime-related properties, CSCs, alloy-family labels, MPESA classification, and source reference for each composition are deposited on Zenodo under the title "CALPHAD-Derived Solidification Properties and CSCs for Ni-, Co-, and Fe-Based Superalloys." https://doi.org/10.5281/zenodo.20145093.

Code availability

The scripts used for descriptor organization, statistical analysis, and visualization are available from the corresponding author upon reasonable request.

Declarations

Conflict of interest

The authors declare that they have no known competing financial interests or personal relationships that could have appeared to influence the work reported in this paper.

References

1. T.M. Pollock, S. Tin, Nickel-based superalloys for advanced turbine engines: chemistry, microstructure and properties. J. Propul. Power **22**(2), 361–374 (2006). https://doi.org/10.2514/1.18239
2. R.C. Reed, *The Superalloys: Fundamentals and Applications* (Cambridge University Press, Cambridge, 2006), p.392. https://doi.org/10.1017/CBO9780511541285
3. J. Hunfeld, H. Sommer, J. Kiese, H. Wang, A. Riyahi Khorasgani, T. Li, C. Somsen, A. Kostka, G. Laplanche, Design of a new wrought CrCoNi-based medium-entropy superalloy C-264 for high-temperature applications. Mater. Des. **211**, 110174 (2021). https://doi.org/10.1016/j.matdes.2021.110174
4. C. Liu, Y. Li, J. Li, Z. Wang et al., A novel low-density and high-strength Fe–Ni-base high-entropy superalloy with stable γ/γ' coherent microstructure at 1023 K. Scr. Mater. **252**, 116236 (2024). https://doi.org/10.1016/j.scriptamat.2024.116236
5. T.-K. Tsao, A.-C. Yeh, J.-W. Yeh, M.-S. Chiou, C.-M. Kuo, H. Murakami, K. Kakehi, High temperature properties of advanced directionally-solidified high entropy superalloys. In: *Superalloys 2016*, 2016 (2016), pp. 1001–1009. https://doi.org/10.1002/9781119075646.ch106
6. T. Saito, A. Ishida, M. Yuyama, Y. Takata, K. Kawagishi, A.-C. Yeh, H. Murakami, Tensile creep behavior of single-crystal high-entropy superalloy at intermediate temperature. Crystals **11**(1), 28 (2021). https://doi.org/10.3390/cryst11010028
7. H.J. Im, D.C. Dunand, Microstructure, hardness, and creep of Co–Fe–Ni-based high-entropy superalloy processed by laser powder-bed fusion. Mater. Sci. Eng., A **916**, 147378 (2024). https://doi.org/10.1016/j.msea.2024.147378
8. S. Xu, M.Y. Araghi, Y. Su, Physics-based modeling of metal additive manufacturing processes: a review. Int. J. Adv. Manuf. Technol. **134**, 1–13 (2024). https://doi.org/10.1007/s00170-024-14156-9
9. M.Y. Araghi, A. Dashti, M. Fani, I. Ghamarian, C. Ruiz, S. Xu, Melt-based additive manufacturing of refractory metals and alloys: experiments and modeling. J. Mark. Res. **37**, 870–892 (2025)
10. T.W. Clyne, G.J. Davies, The influence of composition on solidification cracking susceptibility in binary alloy systems. Br. Foundrym. **74**, 65–73 (1981)
11. H. Yu, J. Liang, Z. Bi, J. Li, W. Xu, Computational design of novel Ni superalloys with low crack susceptibility for additive manufacturing. Metall. Mater. Trans. A **53**(6), 1945–1954 (2022)
12. Thermo-Calc Software, *General Model Library: Crack Susceptibility Coefficient Model. Thermo-Calc Software Documentation* (Thermo-Calc 2024a, 2026). Accessed 8 May 2026
13. J.-O. Andersson, T. Helander, L. Höglund, P. Shi, B. Sundman, Thermo-Calc and DICTRA, computational tools for materials science. Calphad **26**(2), 273–312 (2002). https://doi.org/10.1016/S0364-5916(02)00037-8
14. Z. Han, S. Xia, Z. Chen, Y. Guo, Z. Li, Q. Huang, X.-J. Liu, W.-W. Xu, Facilitated the discovery of new γ/γ' Co-based superalloys by combining first-principles and machine learning. NPJ Comput. Mater. **10**(1), 259 (2024)
15. Y.T. Tang, C. Panwisawas, J.N. Ghoussoub, Y. Gong, J.W. Clark, A.A. Németh, D.G. McCartney, R.C. Reed, Alloys-by-design: application to new superalloys for additive manufacturing. Acta Mater. **202**, 417–436 (2021)
16. Y. Hasebe, T. Hagisawa, C. Yang, K. Aoyagi, K. Yamanaka, A. Chiba, Hot deformation behavior and microstructure of cast Ni-based superalloy IN-100 based on the processing map. Metall. Mater. Trans. A **54**(11), 4456–4471 (2023)
17. E. Akca, A. Gürsel et al., A review on superalloys and IN718 nickel-based INCONEL superalloy. Period. Eng. Nat. Sci **3**(1), 15–27 (2015)
18. S. Zlá, J. Dobrovská, B. Smetana, M. Žaludová, V. Vodárek, K. Konečná, Thermophysical and structural study of IN 792-5A nickel based superalloy. Metalurgija **51**(1), 83–86 (2012)
19. M. Jahangiri, H. Arabi, S. Boutorabi, Development of wrought precipitation strengthened IN939 superalloy. Mater. Sci. Technol. **28**(12), 1470–1478 (2012)
20. D. Karthik, S. Swaroop, Laser shock peening enhanced corrosion properties in a nickel based Inconel 600 superalloy. J. Alloys Compd. **694**, 1309–1319 (2017)
21. S. Utada, L. Despres, J. Cormier, Ultra-high temperature creep of Ni-based SX superalloys at 1250 C. Metals **11**(10), 1610 (2021)
22. H. Bor, C. Chao, C. Ma et al., The influence of magnesium on carbide characteristics and creep behavior of the Mar-M247 superalloy. Scr. Mater. **38**(2), 329–335 (1997)
23. L. Amalia, N. Grain, Y. Su, C.Z. Hargather, S. Xu, P.K. Liaw, Creep in multi-principal element materials—a review. Mater. Today **97**, 103335 (2026)
24. N. Saunders, A.P. Miodownik, eds., *CALPHAD: Calculation of Phase Diagrams: A Comprehensive Guide*. Pergamon Materials Series, vol. 1 (Pergamon, Oxford, 1998), p. 479

25. E.A. Lass, M.E. Williams, C.E. Campbell, K.-W. Moon, U.R. Kattner, Multicomponent γ'-strengthened Co-based superalloys with increased solvus temperatures and reduced mass densities. Acta Mater. **149**, 70–83 (2018). https://doi.org/10.1016/j.actamat.2018.02.027
26. P.M. Mignanelli, N.G. Jones, M.C. Hardy, H.J. Stone, Gamma–gamma prime–gamma double prime dual-superlattice superalloys. Scr. Mater. **136**, 136–140 (2017). https://doi.org/10.1016/j.scriptamat.2017.04.029
27. E. Scheil, Bemerkungen zur schichtkristallbildung. Z. Met. **34**, 70–72 (1942)
28. S. Kou, A criterion for cracking during solidification. Acta Mater. **88**, 366–374 (2015). https://doi.org/10.1016/j.actamat.2015.01.034
29. M.A. Easton, M.A. Gibson, S. Zhu, T.B. Abbott, An a priori hot-tearing indicator applied to die-cast magnesium-rare earth alloys. Metall. Mater. Trans. A **45**, 3586–3595 (2014). https://doi.org/10.1007/s11661-014-2272-7
30. A. Wall, M.J. Benoit, A review of existing solidification crack tests and analysis of their transferability to additive manufacturing. J. Mater. Process. Technol. **320**, 118090 (2023)
31. N. Dupin, B. Sundman, A thermodynamic database for Ni-base superalloys. Scand. J. Metall. **30**(3), 184–192 (2001). https://doi.org/10.1034/j.1600-0692.2001.300309.x
32. Thermo-Calc Software AB, *Thermo-Calc 2022b Release Overview: TCNI12 Nickel-Based Superalloys Database. Thermo-Calc Software Documentation* (Thermo-Calc Software AB, 2022). https://thermocalc.com/news/thermo-calc-2022b-release-overview/. Accessed 28 July 2026
33. H. Mao, H.-L. Chen, Q. Chen, TCHEA1: a thermodynamic database not limited for "high entropy" alloys. J. Phase Equilib. Diffus. **38**(4), 353–368 (2017). https://doi.org/10.1007/s11669-017-0570-7
34. Thermo-Calc Software AB, *Thermo-Calc 2024a Release Overview: TCHEA7 High Entropy Alloys Database. Thermo-Calc Software Documentation* (Thermo-Calc Software AB, 2024). https://thermocalc.com/news/thermo-calc-2024a-release-overview/. Accessed 28 July 2026
35. K.N. Wertz, J.D. Miller, O.N. Senkov, Toward multi-principal component alloy discovery: assessment of CALPHAD thermodynamic databases for prediction of novel ternary alloy systems. J. Mater. Res. **33**(19), 3204–3217 (2018). https://doi.org/10.1557/jmr.2018.61
36. S. Gorsse, O.N. Senkov, About the reliability of CALPHAD predictions in multicomponent systems. Entropy **20**(12), 899 (2018). https://doi.org/10.3390/e20120899

Publisher's Note Springer Nature remains neutral with regard to jurisdictional claims in published maps and institutional affiliations.

Springer Nature or its licensor (e.g. a society or other partner) holds exclusive rights to this article under a publishing agreement with the author(s) or other rightsholder(s); author self-archiving of the accepted manuscript version of this article is solely governed by the terms of such publishing agreement and applicable law.